

A Normalized Framework for the Design of Feature Spaces Assessing the Left Ventricular Function

J. Garcia-Barnés*, D. Gil, L. Badiella, A. Hernández-Sabaté, F. Carreras, S. Pujades, and E. Martí

Abstract—A thorough description of the left ventricle functionality requires combining complementary regional scores. A main limitation is the lack of multiparametric normality models oriented to the assessment of regional wall motion abnormalities (RWMA). This paper covers two main topics involved in RWMA assessment. We propose a general framework allowing the fusion and comparison across subjects of different regional scores. Our framework is used to explore which combination of regional scores (including 2-D motion and strains) is better suited for RWMA detection. Our statistical analysis indicates that for a proper (within interobserver variability) identification of RWMA, models should consider motion and extreme strains.

Index Terms—B-splines, bull's eye plots, left ventricle, manifold parameterization, regional wall motion abnormalities.

I. INTRODUCTION

HEART failure is a prevalent disease [1] that can be caused by various heart conditions, in particular, ischemic heart disease (IHD). The decrease of blood supply produced by coronary artery stenosis impairs the contractile properties of specific myocardial areas. This deviates the normal regional wall motion and contractility patterns of the myocardium, especially the left ventricle (LV) [2]. Early and accurate detection of LV regional wall motion abnormalities (RWMA) might significantly help in the diagnosis and follow-up of IHD [3]. In order to assess the myocardial function, two main issues should be addressed.

- 1) Definition of indicators characterizing the myocardial function, for any patient in a reproducible manner.
- 2) Creation of a statistical model (normality patterns) that is able to discriminate healthy from diseased areas.

A. Myocardial Function Indicators

Clinical routine involves the computation of global indicators such as ventricular volumes, ventricular mass, ejection fraction,

Manuscript received July 06, 2009; revised September 28, 2009; accepted October 04, 2009. Current version published March 03, 2010. This work was supported by the Spanish Projects PI071188, TIN2009-13618, and CONSOLIDER-INGENIO 2010 (CSD2007-00018). The work of D. Gil was supported by The Ramon y Cajal Program. *Asterisk indicates corresponding author.*

*J. Garcia-Barnés is with the Computer Vision Center and the Department of Computer Sciences, Universitat Autònoma de Barcelona, 08193 Bellaterra, Spain (e-mail: jaumegb@cvc.uab.cat).

D. Gil, A. Hernández-Sabaté, and E. Martí are with the Computer Vision Center and the Department of Computer Sciences, Universitat Autònoma de Barcelona, 08193 Bellaterra, Spain (e-mail: debora@cvc.uab.cat).

L. Badiella is with the Servei Estadística UAB, 08193 Bellaterra, Spain.

F. Carreras and S. Pujades are with the Hospital de Sant Pau, 08025 Barcelona, Spain.

Color versions of one or more of the figures in this paper are available online at <http://ieeexplore.ieee.org>.

Digital Object Identifier 10.1109/TMI.2009.2034653

or cardiac output. Their values can be easily obtained from conventional imaging techniques such as echocardiography (EC) or cardiac magnetic resonance (CMR). Although these descriptors give an overall glimpse of the LV global function, they are unable to properly localize RWMA [4].

Since in both EC and CMR, the myocardium appears as a uniform tissue, computation of motion restricts to LV walls deformation. Although wall motion gives a more localized assessment of the ventricular function [5], [6], it is unable to detect RWMA inside the myocardial tissue. Intramural tissue deformation is related to LV rotation, which provides scores (such as twist or circumferential shear) of clinical interest [7].

In order to detect intramural motion of the LV, imaging techniques that induce landmarks inside the myocardium (such as tagged magnetic resonance (TMR) [8], [9] or speckle tracking imaging (STI) [10]) are better suited. TMR prints a grid-like pattern of saturated magnetization over the myocardium. As the pattern evolves by the underlying motion of tissue, it allows visualization and measurement of the intramural deformation. STI assumes that small changes in tissue position lead to corresponding observable changes in the speckles [10], and thus, tracking speckles becomes equivalent to tracking tissue. Motion fields extracted from TMR [11] and STI [7] already constitute an indicator of local function and are used to derive other indicators, such as strains. Strains are well suited to assess the local contractile behavior of the LV since they measure the (local) deformation of an object along a given direction.

B. Comparison Framework

Global clinical scores allow straightforward comparison across patients. However, in the case of local (or regional) values, a faithful comparison should ensure that each image pixel (region) always corresponds to the same anatomical location in the LV for any subject and systolic phase. It follows that comparison of local scores must solve two main artifacts.

- 1) *Inpatient variability* related to the change of LV geometry along the cardiac cycle.
- 2) *Interpatient variability* related to heart's anatomical differences among subjects and the relative position between the patient and the acquisition conditions.

We split current solutions into explicit and implicit approaches.

Explicit approaches use image registration techniques (see [12] for a review) to find the transformation (usually elastic) that best matches images to a reference one. The parameters of such transformations are found by either minimizing the distance between anatomic landmarks [13] or maximizing a similarity criterion between image intensities (e.g., cross correlation [14],

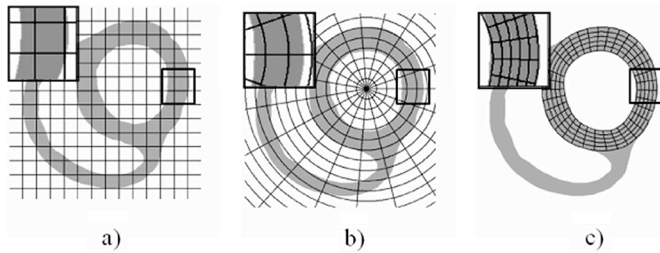


Fig. 1. Regions defined by different coordinates systems used in LV analysis. (a) Cartesian, (b) polar, and (c) local coordinates defined by the normalized parameterization of the LV.

mutual information [15], or a combination of both [16]). Registration approaches have two main weaknesses. On one hand, the election of the reference anatomy might introduce inaccuracies in the registration process if the chosen reference anatomy is an extremum of the population [17]. On the other hand, registration does not provide intuitive coordinates for moving over the LV domain. Since this hinders the definition of anatomical segments, some approaches [15] introduce further processing.

Implicit approaches take place in an abstract level and are based on the subdivision of the LV into segments. By taking into account anatomical features, segments represent portions of tissue consistently defined for any subject, time, and image modality. In this manner, inter- and inpatient LV shape variations are removed and the values in each segment are comparable across subjects. The grounds for LV segment definition were established by the American Heart Association (AHA) [18] in order to standardize LV perfusion and function analysis among different image modalities. Their proposed 17-segment model arises as a tradeoff between anatomical considerations and usability in clinical practice. Although AHA partition has been extensively used [15], [19], [20], some authors [21]–[24] consider more segments in order to provide more continuous approaches.

Segment definition requires coordinate systems adapted to the LV anatomy. The default Cartesian coordinates are not the best suited in the case of curved surfaces like the LV [see the square regions in Fig. 1(a)]. Moreover, vectorial-dependent indicators (such as motion or directional strains) expressed in Cartesian coordinates lack any anatomical meaning. The aforesaid limitations have motivated searching for alternative coordinate systems better adapted to the geometry of the LV. Usual changes include polar coordinates [25] for the 2-D case, and cylindrical [24], [26], [27], spherical [20], [22], planispheric [28], or prolate spheroidal [29], [30] coordinates for the 3-D case. These coordinates define segments better matching the LV geometry [see curved regions given by polar coordinates shown in Fig. 1(b)] and allow expressing motion and strains in clinically meaningful components [27], [28].

Current coordinate systems still present two main shortcomings.

- 1) The regions defined by coordinate directions do not completely fit the LV shape [Fig. 1(b)].
- 2) Coordinates are fixed (usually at end-systole) for all sequence frames, though the LV is an object which deforms along the cardiac cycle.

C. Statistical Models

The ultimate goal of statistical models is to explain the variability of (clinical) attributes (e.g., shape and motion) across a given population. Statistical models are based on analyzing (describing) the values of the attributes on a set of points (landmarks) sampled over the LV domain for several subjects. The set of attributes for all LV points of a given subject constitute a vector called observation. The probability distribution of the observations is commonly assumed to be Gaussian. In this case, the modes of variation are given by principal component analysis (PCA) (like statistical shape models [30] or statistical deformation models [31]). A main drawback is that principal components given by PCA are not well suited for localizing regional abnormalities. Several methods for selecting modes more adapted for RWMA assessment have been proposed. They use multivariate linear regression in [32] to select appropriate principal components, although weak correlation to visual abnormalities was found. Recently, sparse PCA [5] and ICA [33] have reported higher correlations.

One disadvantage of the aforesaid global approaches is that, unless specially designed [30], variation modes lack any clinical meaning. Another disadvantage is that, since they provide a single model for the whole LV, they might require large training sets. An alternative to global methods is to divide the LV in several segments and consider a different model for each of them [22], [34]. On one hand, segmental models are, by design, appropriated for straight evaluation of RWMA and might provide anatomic interpretation by using cardiac coordinate systems. On the other hand, they admit more reduced training sets. This last property allows modeling attributes along cardiac cycle [22], [34] or considering multiple descriptors.

D. Contributions of This Paper

This paper covers two main issues: definition of a general framework allowing comparison across subjects of regional scores and exploration of the subset of local function scores better suited for assessing RWMA.

1) *Comparison Framework*: Following implicit approaches, we present a suitable cardiac coordinate system for the comparison of local scores. We use differential geometry concepts to define a parametrization of the LV domain, considered as a deforming manifold. The parametric map defines a time-evolving coordinate change adapted to each LV anatomy. Such a coordinate system completely unfolds LV geometry onto a (normalized) squared shape, which we call normalized parametric domain (NPD). A main advantage is the straightforward definition of neighborhoods, thus segments, adapted to the LV geometry [Fig. 1(c)].

By taking into account common anatomical features in the definition of the parametrization, we implicitly register LV anatomies in the parametric domain (abstract level). In this manner, the NPD provides a comparison framework for the fusion of local scores of different natures (scalar and vectorial) and their comparison across subjects for a statistical analysis.

2) *Design of Appropriate Feature Spaces for Local Function Assessment*: The NPD is used to fuse several local function indicators (2-D motion and different strains) leading to multi-dimensional descriptors. We adopt a segmental approach and

build a statistical model for each segment. We explore the performance of different configurations of these multidimensional descriptors in order to determine the most appropriate one for RWMA detection. The validity of these models is assessed separately for healthy and pathological population. For the first group, leave-one-out error is used whereas, for the second one, the ability to detect injured regions is evaluated using ground truth maps provided by several experts. Our statistical analysis suggests that motion and extreme strains should be taken into account.

The paper is organized as follows. In Section II, we define the NPD comparison framework, and in Section III, we build it for the particular case of the LV in SA view. Regional multivariate function descriptors are defined in Section IV-A and functional assessment in Section V. Experimental settings and results are presented in Sections VI and VII, respectively. Finally, discussion and future work are given in Sections VIII and IX, respectively.

II. NORMALIZED PARAMETRIC DOMAIN

Statistical analysis of regional scores requires defining segments adapted to the LV anatomy consistently identified across subjects and systolic times. As suggested in [35], we will parameterize the LV domain in the sense of differentiable manifolds with boundary [36].

An n -dimensional manifold is a mathematical object that, seen on a small enough scale, is isomorphic (i.e., identifies) to the n -dimensional Euclidean space, \mathbb{R}^n . Intuitively, a manifold can be built by doing “patchwork”. That is, it can be covered by “cutting” pieces of \mathbb{R}^n , “deforming” them, and smoothly “gluing” them together one by one. Each piece of \mathbb{R}^n , namely Ω , is called parametric domain and the deformation, namely Ψ , parametric map or parameterization. The mapping Ψ warps the parametric domain Cartesian coordinates onto parametric curves (locally) describing the manifold geometry [see curves in Fig. 1(c)].

Although, in general, a single domain Ω is not enough to cover all the manifold, most anatomic structures are isomorphic to shapes (tubes for vessels, ellipsoids for the LV domain, torus for the LV in SA views) admitting a single-domain parameterization. In the case of the LV in SA view, since it is diffeomorphic [36] to a torus, the parametric domain is given by its circumferential (u) and radial (w) coordinates.

The parametric coordinates define for each subject a mapping, $\Psi = \Psi(u, w) = (\Psi_x(u, w), \Psi_y(u, w))$, between the unitary cube and any LV domain (noted by \mathcal{LV})

$$\Psi : \Omega = [0, 1] \times [0, 1] \longrightarrow \mathcal{LV}. \quad (1)$$

In this case, we call Ω NPD.

The map Ψ defines a coordinate change that registers any \mathcal{LV} to a template, Ω , which is an unfolded version of the \mathcal{LV} . In contrast to other coordinate changes [such as polar coordinates in Fig. 1(b)], Ψ ensures that the new coordinate curves completely fit the LV geometry [see Fig. 1(c)]. Besides, since \mathcal{LV} is completely straightened in the NPD, coordinate curves become straight lines (the Cartesian axis of Ω).

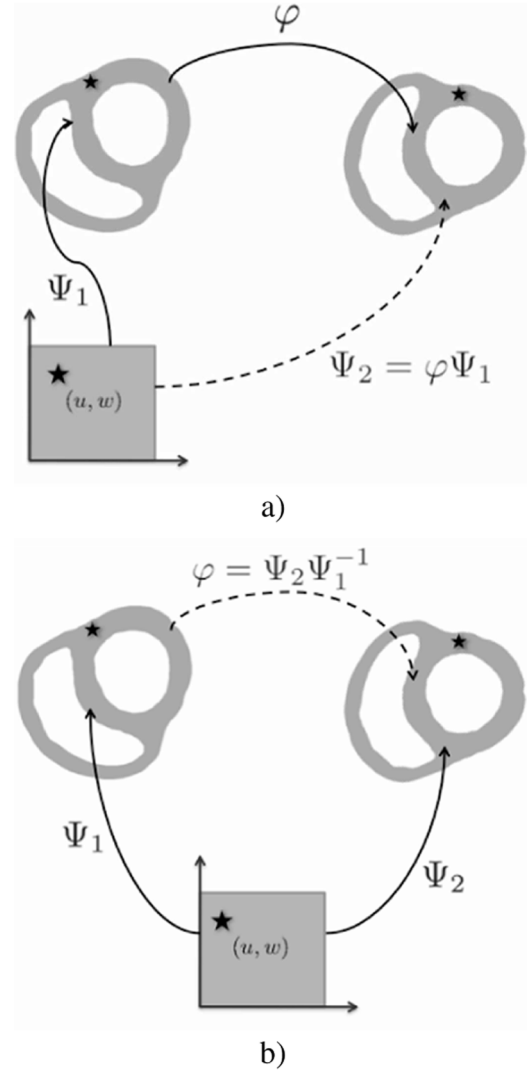


Fig. 2. Implicit registration in the NPD: (a) common parametric domain for two diffeomorphic manifolds and (b) implicit registration given by a common parametric domain.

For any two LV domains, $\mathcal{LV}_1, \mathcal{LV}_2$, there is always (by means, for instance, of explicit registration techniques) a transformation, φ , that deforms one domain into the other one. Such transformation allows the definition of a parameterization (Ψ_1 for \mathcal{LV}_1 and the composition $\Psi_2 := \varphi\Psi_1$ for \mathcal{LV}_2) that assigns equal parameters to corresponding anatomical locations [see Fig. 2(a)]. Thus, if a parameterization map is defined such that it assigns the same parameter (u, w) to anatomical locations consistently defined for any \mathcal{LV} , the two LVs are registered in two ways. On one hand, the maps Ψ_1, Ψ_2 provide an implicit registration between \mathcal{LV}_1 and \mathcal{LV}_2 in the NPD. On the other hand, the composition $\Psi_2\Psi_1^{-1}$ explicitly registers the LV domains in Euclidean (image) space. Fig. 2(b) illustrates the implicit registration given by two parameterizations labeling same anatomical locations (\star) with the same parameter (u, v). Parameters ensuring registration can be defined by assigning specific parametric values to the same localized anatomic structures common to all subjects. In particular, Ω boundaries should map

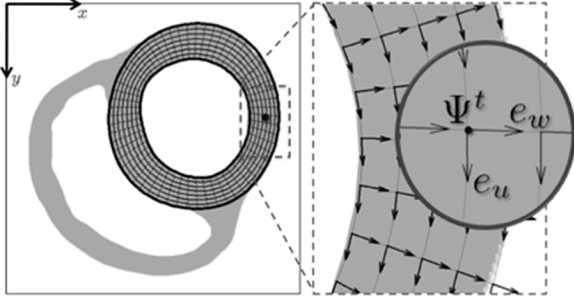


Fig. 3. Local coordinate systems $\{e_u, e_w\}$ (along circumferential and radial directions, respectively) induced by the parametrization Ψ .

to \mathcal{LV} walls (endocardium and epicardium) and the septal segment to the same angular range.

A. Mapping Data to the NPD

Local clinical scores can be either vectorial (motion fields, denoted by \vec{V}) or scalar (strains, denoted by S) values defined on each point on \mathcal{LV} . In order to compare such measurements across different patients, they must be mapped to the NPD.

In the case of scalar scores, they are directly mapped by computing them at the points $\Psi(u, v)$. That is, it suffices to consider $S(\Psi(u, v)), \forall (u, v) \in \Omega$. Unlike scalar data, displacement vectors are expressed in image coordinates. These global coordinates depend on acquisition conditions that, in general, vary across patients. In order to get intrinsic coordinates, vectorial data should be expressed in terms of the local references associated to the \mathcal{LV} parameterization.

Vector mapping is done by applying the Jacobian of the parameterization. Instead of using the Jacobian of the inverse map [31], we decompose [36] the deformation vectors into their circumferential (corresponding to the u coordinate) and radial (corresponding to the w coordinate) components. The coordinates of the local parametric vectors are given by the columns of the Jacobian of the parameterization

$$D\Psi = (\nabla_u \Psi, \nabla_w \Psi) = \begin{pmatrix} \partial_u \Psi_x & \partial_w \Psi_x \\ \partial_u \Psi_y & \partial_w \Psi_y \end{pmatrix} \quad (2)$$

for ∂_u, ∂_w denoting Ψ partial derivatives with respect to u and w . The columns of the Jacobian define, for each $p \in \mathcal{LV}$, a nonorthogonal (local) reference of unitary vectors $\{e_u, e_w\}$ describing the local geometry of the \mathcal{LV} domain

$$e_u = \frac{\nabla_u \Psi}{\|\nabla_u \Psi\|_2} \quad e_w = \frac{\nabla_w \Psi}{\|\nabla_w \Psi\|_2} \quad (3)$$

for $\|\cdot\|_2$ the Euclidean norm. Fig. 3 shows the description of \mathcal{LV} geometry given by $\{e_u, e_w\}$.

By linearity of the tangent application, the components of V in terms of the local references

$$V = V_u e_u + V_w e_w \quad (4)$$

give the mapping of V onto Ω . We will call V_u and V_w circumferential and radial components, respectively.

B. Properties of the NPD Framework

The NPD framework provides, both, a subject-specific cardiac coordinate system and an implicit registration to a normalized squared template.

Although existing cardiac coordinate systems (prolate spheroidal, cylindrical, etc.) might be called parameterizations, they do not actually parameterize the LV domain from the point of view of differential geometry. This follows from the fact that coordinate curves do not fit the LV geometry, but other geometries [like circles in Fig. 1(b)] roughly approximating the LV true geometry. Our parameterization-based approach has the following advantages over existing cardiac coordinate systems.

- 1) *Definition of \mathcal{LV} segments/regions adapted to the subject-specific anatomy.* Since, by definition, coordinate curves faithfully describe the LV geometry, segments adapted to the \mathcal{LV} geometry are defined by means of a rectangular grid in Ω .
- 2) *Local operations.* Local operations, such as interpolation or smoothing, along \mathcal{LV} geometry can be done along the rectangular axis of Ω , which correspond to vertical (rows) and horizontal (columns) directions.
- 3) *Anatomical interpretation of vector-dependant scores.* Vectorial quantities expressed in the local reference system given by (3) have a clinical interpretation in terms of the \mathcal{LV} anatomy.
- 4) *Visualization.* Values at Ω can be easily mapped to bull's eye plots for a better visual interpretation of results.

On the other hand, our parameterization-based implicit registration enjoys several advantages over explicit registration schemes.

- *Generic comparison framework.* The NPD provides a comparison domain (Ω) well suited for comparing and fusing different local and segmental scores.
- *Generic abstract template of the \mathcal{LV} .* Since LV anatomies are registered to a common domain, NPD overcomes the problem (in registration approaches) of choosing a reference anatomy [17]. In fact, the NPD might be considered as an abstract version of the natural coordinates proposed in [17].
- *Identification of specific anatomic locations.* The parameter assignment required for implicit registration allows localizing any anatomical point with respect to \mathcal{LV} boundaries and the septal segment. This provides a way of moving on the LV intuitive for physicians.

III. BUILDING THE NPD OF THE LEFT VENTRICLE

The superscript t will indicate a given systolic phase. Thus, \mathcal{LV}^t and Ψ^t will stand for a generic LV domain and its parameterization at time t . In the case of several subjects, the subscript n will be used to identify them. A 2-D point in the image will be noted for short by \mathbf{x} and end-systolic time by T_{ES} . Since T_{ES} depends on the subject, we will use T_{ES_n} .

We propose using the segmentation of the LV boundaries [35] to obtain the parameterization Ψ^t using B-splines in a twofold process. First the initial parameterization Ψ^0 is defined at end diastole (given by the first frame). Next, Ψ^t is defined by updating using motion maps. The motion vector field between frame $t-1$

and frame t will be noted by V^t and it is computed from TMR sequences using the harmonic phase flow (HPF) method [37].

A. \mathcal{LV}^0 Parameterization

The parameterization of \mathcal{LV}^0 splits in four steps.

- Step 1) *Landmark identification.* The inner (endocardium) and outer (epicardium) contours of \mathcal{LV}^0 are extracted and anatomical key points are located.
- Step 2) *Anatomical affine reference.* An affine coordinate system based on \mathcal{LV}^0 anatomy is defined in order to account for variability in patient–device relative position.
- Step 3) *Boundaries parameterization.* B-spline curves are fitted to endocardial and epicardial contours in the new affine reference in order to account for anatomic changes across patients and deformations due to heart beating.
- Step 4) *Domain parameterization.* Finally, the parametric map is obtained by fitting a bidimensional B-spline to the domain defined by \mathcal{LV}^0 boundaries.

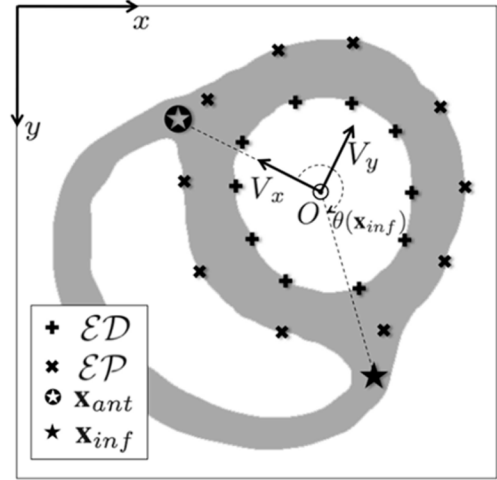
1) *Step1: Landmark Identification:* Identification of anatomical landmarks is required for defining the anatomic reference and the circumferential parameter.

The set of \mathcal{LV}^0 boundary points will be denoted by \mathcal{ED} for the endocardium and \mathcal{EP} for the epicardium. Following [38], we manually identify them at positive times and track them back to $t = 0$ using HPF. The number of points depends on the number of control points (linked to the degree of the blending functions) used for the B-spline. In our case, we use 12 for, both, endocardium and epicardium.

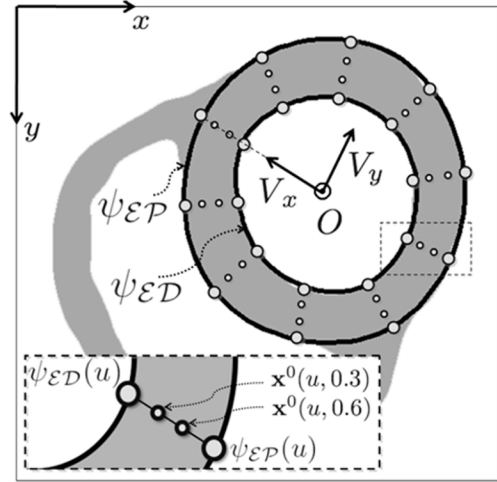
We also identify the junction points between left and right ventricles at anterior (\mathbf{x}_{ant}) and inferior (\mathbf{x}_{inf}) LV walls, respectively [Fig. 4(a)]. These two points are used in the definition of the affine reference system accounting for affine variability in patient–device relative position. Their angular coordinates in such affine systems serve to define the (average) portion of septal wall, G . Such value is taken into account for the definition of the angular coordinate (u) in order to register \mathcal{LV} anatomies. Since the points \mathbf{x}_{ant} , \mathbf{x}_{inf} should only indicate anatomic directions, they do not necessarily belong to the sets \mathcal{ED} and \mathcal{EP} .

2) *Step2: Anatomical Affine Reference:* An affine coordinate system is defined by means of an origin of coordinates, O , and two linearly independent axes, V_x and V_y . The new origin is defined as the center of mass of \mathcal{ED} in order to compensate any translation among different subjects. The new x -axis, V_x , is a unitary vector starting at O and pointing to \mathbf{x}_{ant} . Finally, V_y is a unitary vector orthogonal to V_x and oriented oppositely to the septal wall. Since V_x points the same anatomical location for any LV, by setting V_x as the origin of angles, we handle any rotational disparity among different subjects. The scheme in Fig. 4(a) shows the anatomical reference defined by the anatomical landmarks in comparison to the image coordinate axis (upper left corner).

3) *Step3: \mathcal{LV}^0 Boundaries Parameterization:* We compute a unified compact parameterization of \mathcal{LV}^0 boundaries by fitting (in the least-squares sense [39]) a couple of B-spline curves to \mathcal{ED} and \mathcal{EP} , expressed in the anatomic affine system [Fig. 4(b)].



(a)



(b)

Fig. 4. \mathcal{LV}_0 parameterization. (a) Landmark identification (\mathcal{ED} , \mathcal{EP} , \mathbf{x}_{ant} , and \mathbf{x}_{inf}) for the definition of the affine reference. (b) \mathcal{LV}_0 boundaries parameterization and interpolation of intramural points, $\mathbf{x}^0(u, w)$.

B-splines are defined by a normalized circumferential parameter, $u \in [0, 1]$, ensuring implicit registration of \mathcal{LV}^0 across subjects.

Anatomic (implicit) registration is achieved by assigning a circumferential range $[0, G]$ to nonseptal segments and $[G, 1]$ to the septal one. The transition parameter G is computed as the normalized average of the angular coordinate, $\theta \in [0, 2\pi]$, of \mathbf{x}_{inf} in the system $\{O, V_x, V_y\}$ for Q healthy volunteers

$$G = \frac{1}{2\pi Q} \sum_{q=1}^Q \theta(\mathbf{x}_{inf}^q). \quad (5)$$

The normalized angular coordinate u is defined as

$$u(\mathbf{x}) = \begin{cases} \frac{G}{\theta(\mathbf{x}_{rminf})} \theta(\mathbf{x}), & \theta(\mathbf{x}) \leq \theta(\mathbf{x}_{inf}) \\ \frac{(1-G)(\theta(\mathbf{x})-1)}{2\pi-\theta(\mathbf{x}_{inf})} + 1, & \theta(\mathbf{x}) > \theta(\mathbf{x}_{inf}). \end{cases} \quad (6)$$

A couple of closed cubic B-spline curves, $\psi_{\mathcal{ED}}$, $\psi_{\mathcal{EP}}$, are fitted to the boundary points \mathcal{ED} and \mathcal{EP} by minimizing

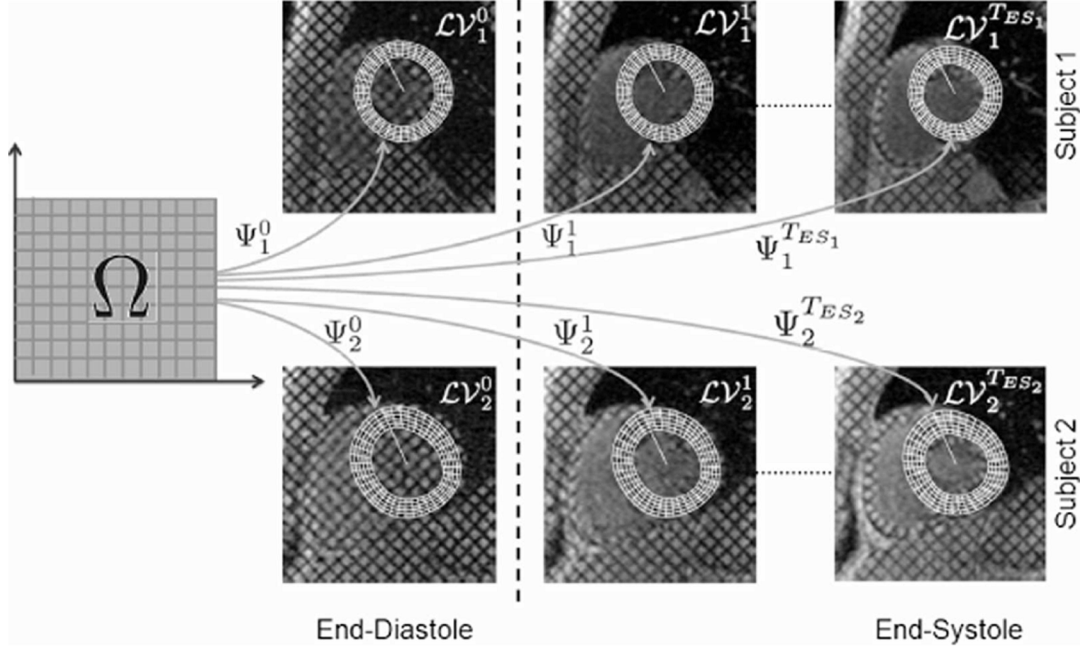


Fig. 5. Implicit registration of two TMR sequences belonging to different subjects. Each parameterization Ψ_n^t defines a coordinate system tailored for the geometry of each subject and time. Same anatomical locations share the same parameter in Ω .

$$\sum_{\mathbf{x} \in \mathcal{E}\mathcal{D}} \|\psi_{\mathcal{E}\mathcal{D}}(u(\mathbf{x})) - \mathbf{x}\|^2 + \sum_{\mathbf{x} \in \mathcal{E}\mathcal{P}} \|\psi_{\mathcal{E}\mathcal{P}}(u(\mathbf{x})) - \mathbf{x}\|^2. \quad (7)$$

4) *Step4: $\mathcal{L}\mathcal{V}^0$ Domain Parameterization:* In order to get the final parameterization, $\Psi^0(u, w)$, we fit a bidimensional spline to a uniform sampling of the radial values (normalized in the range $[0, 1]$) of the two border splines. Since at end-diastole tissue does not have any deformation, the radial direction can be linearly sampled [20] as

$$\mathbf{x}^0(u, w) = \psi_{\mathcal{E}\mathcal{D}}(u)w + \psi_{\mathcal{E}\mathcal{P}}(u)(1 - w), \quad (u, w) \in \Omega. \quad (8)$$

We evaluate the aforesaid equation at a $N_u \times N_w$ uniform grid in Ω given by $u_i = (i - 1)/(N_u - 1)$ and $w_j = (j - 1)/(N_w - 1)$. This provides $N_u \times N_w$ myocardial points, $\{\mathbf{x}_{ij}^0\}_{i,j=1}^{N_u, N_w}$, at the initial time. These points are equiangular in the circumferential direction for each segment (septal and nonseptal) and equidistant in the radial one. Fig. 4(b) shows a sampling of the parameterized boundaries $\psi_{\mathcal{E}\mathcal{D}}$ and $\psi_{\mathcal{E}\mathcal{P}}$ given by a grid of 10×4 points. The close-up illustrates the linear interpolation of radial positions (intramural points $\mathbf{x}^0(u, w)$) at $w = 0.33$ and $w = 0.66$ from boundary points sharing same circumferential parameters.

The parametric map is obtained by fitting a bidimensional B-spline surface to the set $\{\mathbf{x}_{ij}^0\}_{i,j=1}^{N_u, N_w}$. The B-spline surface is given by

$$\Psi^0(u, w) = \sum_{r=1}^{M_u} \sum_{s=1}^{M_w} R_r(u) S_s(w) P_{rs} \quad (9)$$

for R_r cubic blending functions, S_s quadratic blending functions, and $P_{rs} \in \mathbb{R}^2$ $M_u \times M_w$ control points ensuring a closed surface along the circumferential direction. Blending functions

in the radial direction are chosen quadratic because image resolution does not guarantee enough information along this direction. Control points are given by minimizing

$$\sum_{i=1}^{N_u} \sum_{j=1}^{N_w} \|\Psi^0(u_i, w_j) - \mathbf{x}_{ij}^0\|^2. \quad (10)$$

B. $\mathcal{L}\mathcal{V}^t$ Parameterization

The domain $\mathcal{L}\mathcal{V}^t$ is parameterized by fitting a B-spline surface to a set of points, \mathbf{x}_{ij}^t , sampled on the $\mathcal{L}\mathcal{V}^t$ domain. Such points are obtained by iteratively applying the displacement between consecutive frames, \vec{V}^t , to the points \mathbf{x}_{ij}^0

$$\mathbf{x}_{ij}^t = \begin{cases} \mathbf{x}_{ij}^0, & t=0 \\ \mathbf{x}_{ij}^{t-1} + \vec{V}^{t-1}(\mathbf{x}_{ij}^{t-1}), & t > 0. \end{cases} \quad (11)$$

The mapping Ψ^t is the minimum of the cost functional given by changing \mathbf{x}_{ij}^0 for \mathbf{x}_{ij}^t in (10). By keeping the parameters (u_i, v_j) unchanged for any sequence and time, we ensure the implicit registration requirement of Section II. Fig. 5 sketches the parameterization of the LV domain along the whole systolic cycle for two different subjects.

IV. MULTIVARIATE REGIONAL FUNCTION DESCRIPTORS

Following [19], in order to assess myocardial local function, we consider two different kinds of local indicators: zeroth-order (motion) and first-order (strains). Since their comparison and fusion take place in the NPD, all attributes are considered at the points $\mathbf{x} = \Psi^t(u, w)$.

A. Local Function Descriptors

1) *Zeroth-Order Indicators (Motion):* Motion is given by the (two) components, (V_x^t, V_y^t) , of the vector fields V^t expressed

in image coordinates. Our zeroth-order attributes are given by the circumferential (V_u^t) and radial (V_w^t) components [given by formula (4)] of the motion vectors V^t .

2) *First-Order Indicators (Strains)*: They are given by the spatial variations (first partial derivatives) of the displacement maps and are computed by means of the strain tensor

$$E(V) = \frac{1}{2} (\nabla V + \nabla V^T + \nabla V^T \nabla V) \quad (12)$$

where

$$\nabla V = \begin{pmatrix} \partial_x V_x & \partial_y V_x \\ \partial_x V_y & \partial_y V_y \end{pmatrix} \quad (13)$$

and T denotes the transpose of a vector or matrix. The strain at a point \mathbf{x} along a direction v (with $\|v\| = 1$) is given by

$$S_v(\mathbf{x}) = v^T E(V(\mathbf{x})) v. \quad (14)$$

Strains describe the amount of contraction the muscle undergoes. In cardiac function analysis, the usual strains are extremal (minimal, S_m , and maximal, S_M) strains and directional strains. The latter are commonly computed along radial (S_R) and circumferential (S_C) directions. In addition, we also consider the strain along the direction of displacement (S_D). Extremal strains are given by the highest (S_M^t) and the lowest (S_m^t) eigenvalues of the strain tensor evaluated in the NPD, $E(V^t(\mathbf{x}))$. Directional strains are given by

$$\begin{aligned} S_D(\mathbf{x}) &= \frac{V^t(\mathbf{x})^T}{\|V^t(\mathbf{x})\|} E(V^t(\mathbf{x})) \frac{V^t(\mathbf{x})}{\|V^t(\mathbf{x})\|} \\ S_C(\mathbf{x}) &= (e_u(\mathbf{x}))^T E(V^t(\mathbf{x})) e_u(\mathbf{x}) \\ S_R(\mathbf{x}) &= (e_w(\mathbf{x}))^T E(V^t(\mathbf{x})) e_w(\mathbf{x}) \end{aligned} \quad (15)$$

for e_u, e_w given by the (3)

B. Time and Space Normalization

In order to obtain quantities comparable across different studies, spatiotemporal variability across acquisitions should be compensated. On one hand, TMR studies may have different spatial resolution. On the other hand, due to heart beat variability, the number of frames per cardiac cycle differs from one study to another.

1) *Space Normalization*: Since TMR studies may have different spatial resolution (depending on the acquisition conditions), the displacement vector fields in pixels are noncomparable. This artifact is removed by considering motion fields in millimeter. Millimeter resolution is achieved by resizing images so that 1 pixel corresponds to 1 mm².

2) *Time Normalization*: Temporal resolution is compensated by interpolating the motion components V_x^t and V_y^t in order to get a uniform sampling along the systolic cycle for all subjects. Let us consider the discrete sets $\{V_x^t(\mathbf{x})\}_{t=0}^{T_{ES_n}}$ and $\{V_y^t(\mathbf{x})\}_{t=0}^{T_{ES_n}}$. The components at time $t = 0$ correspond to 0% of systolic cycle, whereas components at time $t = T_{ES_n}$ correspond to 100% of systole. We resample values (by using

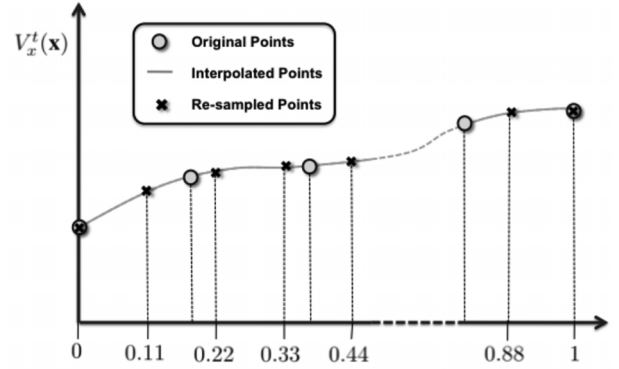


Fig. 6. Temporal normalization the component of the motion field V_x .

cubic interpolation) at N_T uniformly sampled fractions of the systolic cycle given by $t = \{kT_{ES_n}/NT\}_{k=0}^{NT}$.

Fig. 6 shows the resampling process of the x component V_x^t at a given point \mathbf{x} . The x -axis represents the fraction of systolic cycle. The components obtained from analysis of TMR sequences, $\{V_x^t(\mathbf{x})\}_{t=0}^{T_{ES_n}}$, are plotted in circles. The values at the uniform sampling of the systolic cycle are plotted in crosses over the interpolated curve in solid line.

C. Multivariate Regional Descriptors

Usually zeroth- and first-order attributes are considered separately. However, on one hand, strains reflect muscle contraction at an image plane. On the other hand, since tissue motion might follow from adjacent contracting fibers (dragging effect), motion might reflect the dynamic behavior of areas even outside the image plane. We, thus, consider that by taking into account both attributes, better descriptors reflecting (in spite of being 2-D) the 3-D functionality of the LV should be obtained. Merging all the attributes described so far, we obtain a 9-D feature space describing the LF of the LV

$$\Gamma^t(\mathbf{x}) = [V_u^t(\mathbf{x}), V_w^t(\mathbf{x}), S_C^t(\mathbf{x}), S_R^t(\mathbf{x}), S_D^t(\mathbf{x}), S_M^t(\mathbf{x}), S_m^t(\mathbf{x})]. \quad (16)$$

The multivariate descriptor (15) provides a pointwise robust (from the statistics point of view) representation of the \mathcal{LV} function that we next analyze within regions. Regions along the circumferential direction are called sectors whereas along the radial direction layers.

Regions in the LV are defined by giving a uniform grid on Ω defining grid cell corners. A sampling given by $u_I = \{(I-1)/N_S\}_{I=1}^{N_S}$ and $w_J = \{(J-1)/N_L\}_{J=1}^{N_L}$ divides Ω in N_S sectors and N_L layers, whose regions, ω_{IJ} , are defined as

$$\omega_{IJ} = \{(u, w) \in \Omega / u_I \leq u \leq u_{I+1}, w_J \leq w \leq w_{J+1}\}.$$

The functional behavior at each ω_{IJ} for a given systolic time t is given by the average

$$\Gamma_{IJ}^t := \frac{1}{N_u N_w} \sum_{i=1}^{N_u} \sum_{j=1}^{N_w} \Gamma^t(\Psi^t(u_i, w_j)) \quad (u_i, w_j) \in \omega_{IJ}$$

for (u_i, w_j) a uniform sampling over ω_{IJ} .

V. REGIONAL FUNCTION ASSESSMENT

Regional normality models follow from the statistical analysis of the descriptors $\{\Gamma_{IJ}^t\}_{t=1}^{N_T}$ obtained for healthy volunteers. In this paper, we assume Gaussianity and describe the regional normal function of the LV with $N_L \times N_S \times N_T$ Gaussian models (one for each spatiotemporal region). Principal component analysis serves to obtain the orthogonal basis that best explains the correlations among functional parameters. The eigenvectors of the covariance matrix of the observations give the modes of variation and the eigenvalues of the expected normal ranges.

Let $\mu_{IJ}^t, \Sigma_{IJ}^t$ be, respectively, the mean and covariance matrix of Γ_{IJ}^t for healthy cases. Given an incoming subject, the Mahalanobis distance

$$dM_{IJ}^t = \sqrt{(\Gamma_{IJ}^t - \mu_{IJ}^t)^T (\Sigma_{IJ}^t)^{-1} (\Gamma_{IJ}^t - \mu_{IJ}^t)}$$

quantifies the deviation of the subject regional descriptor Γ_{IJ}^t from the average healthy model. The average of dM_{IJ}^t for all times

$$\mathcal{D}_{IJ} = \frac{1}{N_T} \sum_{t=1}^{N_T} dM_{IJ}^t \quad (17)$$

gives a compact description of the region's integrity. Regions are considered "Abnormal" if \mathcal{D}_{IJ} is over a given threshold Th and "Normal" otherwise. The threshold value was set using receiver operating characteristic (ROC) analysis, as detailed in Section VII.

A. Parametric Images

For the visualization of the different regional data that have been generated, we use bull's eye plots (BEPs). BEPs are polar plots that represent an idealized shape of the LV. The most extended BEP is the standardized 17-segment division suggested by the AHA [18]. AHA BEPs plot four SA levels (basal, mid, apical, and apical cup) in the same four four-ring chart [one ring per SA level, as shown in Fig. 7(a)]. Following other works [21]–[24], [40], we prefer using our own-developed division. We use a separate BEP for each of our SA levels (basal, mid, and apex). Each BEP is divided into $N_L \times N_S$ sectors and an arc representing the septal portion is displayed on the left. For each BEP, the outer rim denotes epicardium (except for the septum, where it denotes RV endocardium) and the inner rim denotes endocardium. For a better comparison to AHA segments, they are shown labeled as follows. A stands for *Anterior*, AL for *Anterolateral*, IL for *Inferolateral*, I for *Inferior*, IS for *Inferoseptal*, and AS for *Anteroseptal*. Fig. 7(b)–(d) shows our bull's eye charts for base, mid, and apex, respectively.

Each sector is colored according to its classification: green is used for "Normal" regions and red for "Abnormal" ones. In order to obtain a more descriptive assessment, the red (R) and green (G) channels are colored according to Table I. In this manner, dark colors indicate (for, both, "Normal" and "Abnormal") values close to the boundary discriminating pathological behaviors from normal ones. Meanwhile, bright tones correspond to extreme behaviors: severe deviation from normality

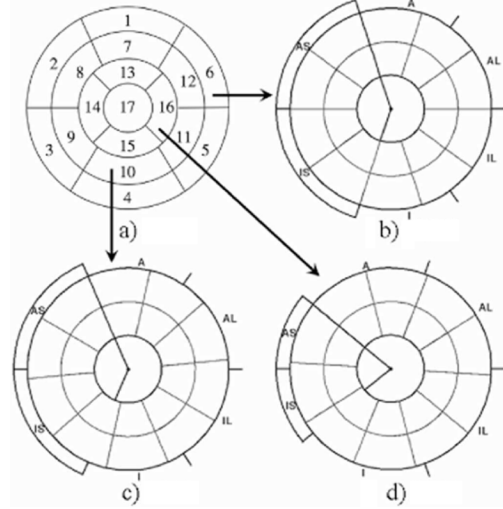


Fig. 7. Different bull's eye charts. (a) AHA LV representation in the four levels, 17 segments. (b)–(d) Segments 1–6 correspond to a basal cut, 7–12 to a midcut, 13–16 to an apical cut, and 17 (optional) to the apex. Our representation for basal, mid, and apical levels. (a) AHA. (b) BASE. (c) MID. (d) APEX.

TABLE I
VISUALIZATION OF REGIONAL FUNCTION ASSESSMENT

Function Value	Label	Color
$\mathcal{D}_{IJ} < Th$	'Normal'	$R = 0; G = \frac{e^{-\mathcal{D}_{IJ}/2} - e^{-1}}{1 - e^{-1}}; B = 0$
$\mathcal{D}_{IJ} > Th$	'Abnormal'	$R = \frac{e^{-1} - e^{-\mathcal{D}_{IJ}/2}}{e^{-1}}; G = 0; B = 0$

TABLE II
PARAMETER CONFIGURATIONS USED IN OUR EXPERIMENTS

\mathcal{C}	V_u	V_w	S_C	S_R	S_D	S_M	S_m	Dim
1	•	•	–	–	–	–	–	2
2	–	–	•	•	–	–	–	2
3	–	–	–	–	–	•	•	2
4	•	•	–	–	•	–	–	4
5	•	•	•	•	–	–	–	4
6	•	•	–	–	–	•	•	4
7	•	•	•	•	•	–	–	5
8	•	•	–	–	–	•	•	5
9	•	•	•	•	•	•	•	7

for the red color and high agreement to normal function for the green one.

VI. EXPERIMENTAL SETTING

The NPD framework has been applied to assess the regional systolic function in TMR sequences. For each sequence, $N_L \times N_S \times N_T = 2 \times 10 \times 9$ spatiotemporal regions have been considered. The 7-D feature space defined in (15) is explored in order to determine which subsets of parameters are best suited for regional assessment of LV function. Among the 127 possible configurations, we have analyzed nine representative subsets ($\mathcal{C}_i, i = 1, \dots, 9$) given in Table II. The bullet indicates that a particular attribute is present in the configuration.

For each configuration we have assessed the following.

- 1) *Model Consistency*. We consider that for healthy cases, all regions should be labelled as "Normal." Consistency is assessed by leave-one-out (LOO) errors for the volunteers data set.

- 2) *Pathology Discrimination*. The clinical potential is given by the ability for detecting anomalous regional behaviors. Discrimination is assessed by comparing the automatic classification to manual labeling.

A. Experimental Data Set

Our data set consists of healthy volunteers and patients with several degrees of hypokinesis.

- 1) *Healthy subjects*. Composed of a total number of 21 volunteers, 15 males and 6 females aged between 23 and 55 (30.7 ± 7.5).
- 2) *Nonhealthy subjects*. Composed of a total number of seven patients (six infarcted and one hypertrophic), four males and three females aged between 47 and 71 (60 ± 8).

For each subject, TMR sequences at basal, mid, and apical levels were recorded in breath-hold. The acquisition device was a Siemens Avanto 1.5 T (Erlangen, Germany) with a spatial resolution from 1.3×1.3 to 1.7×1.7 mm/pixel and temporal resolution within 5–8 frames/syst. cycle.

B. Ground Truth Maps

For each sequence, we define its ground truth as a BEP chart with each of its $N_L \times N_S$ regions labeled as “Normal” or “Abnormal” (BEPs labeled *Expert#1* and *Expert#2* in Fig. 10). Physicians were asked to visually identify those regions moving abnormally. The expert was given two TMR sequences: the original one and another with the $N_L \times N_S$ time-evolving regions printed over \mathcal{LV}^t . A region was labeled “Abnormal” if it presented any anomalous behavior along the systolic cycle. Two different experts have been considered in order to compute interobserver variability.

C. Quality Scores

The performance of each configuration was evaluated in terms of sensitivity and specificity given by

$$\text{spec} = \frac{T_N}{N}, \quad \text{sens} = \frac{T_P}{P} \quad (18)$$

for T_P true positives (number of regions correctly classified as “Abnormal”) and T_N true negatives (number of regions correctly classified as “Normal”). The total number of “Abnormal” (positive) and “Normal” (negative) regions are P and N . We are particularly interested in minimizing sensitivity.

Consistency is given by LOO errors. For each configuration, the normality model is computed using all healthy cases except one, which is used as test. The process is repeated for each healthy subject and the false positive rate ($1 - \text{sens}$) is computed at each round. We define our measure of consistency as the average of LOO errors for the sequences of all healthy cases. The threshold Th is defined by the radius of the ellipsoid containing 95% of the normal samples. In this manner, the consistency error should be around 5%. Any increase might be attributed to errors in the computation of the statistical model parameters. It follows that \mathcal{E}_C indicates the maximum number of dimensions that can be reliably modeled with a given number of healthy samples. The threshold value is $\text{Th} = 2.4$ for two dimensions ($\mathcal{C}_1 - \mathcal{C}_3$),



Fig. 8. Leave-one-out errors for the nine parameter configurations.

$\text{Th} = 2.8$ for three dimensions (\mathcal{C}_4), $\text{Th} = 3.1$ for four dimensions (\mathcal{C}_5 and \mathcal{C}_6), $\text{Th} = 3.35$ for five dimensions (\mathcal{C}_7 and \mathcal{C}_8), and $\text{Th} = 4.1$ for seven dimensions (\mathcal{C}_9).

Concerning discriminant capability, we will check the ability of the system to perform as a human expert. Since manual labeling of sequences is prone to vary across experts, the system will perform as one of them if classification errors compare to interobserver variability [41]. Interobserver variability (sensitivity and specificity) is computed by taking one of the experts labeling as ground truth and the other one as configuration output. ROC curves are used to define the optimal cutoff threshold Th . We define the cutoff value as the radius that achieves the same sensitivity as interobserver sensitivity, which is 0.7732 in our case. Since we have one ROC curve for each expert, the cutoff Th is given by the average of the cutoff values for both experts. This optimal Th is used to assess each configuration. We have considered the following agreement measures between each configuration and expert: area under ROC curve (AUC), Spearman rank correlation (Corr) [42], specificity, sensitivity, and confidence intervals (CI) for mean differences. Agreement scores have been computed using stratified-by-sequence analysis. Results for each sequence were aggregated in order to obtain confidence intervals and standard errors (given by mean \pm standard deviation) using sequences as experimental unit. In this manner, agreement measures incorporate intersequence variability.

VII. EXPERIMENTAL RESULTS

A. Model Consistency

Fig. 8 shows the graphic of bars for model consistency for the nine configurations. By the choice of the threshold (including 95% of the healthy population) errors should be around 5%. Configurations ($\mathcal{C}_1 - \mathcal{C}_4$) under 4-D are the only spaces fulfilling such condition. 4-D configurations (\mathcal{C}_5 , \mathcal{C}_6) rise to 10% and higher dimensional spaces reach errors over 20%. For equal dimension, we observe a worse performance in configurations including directional strains (\mathcal{C}_2 , \mathcal{C}_5 , and \mathcal{C}_7).

B. Pathology Discrimination

Fig. 9 shows ROC plots for the nine configurations. Each plot shows the ROC curves for the two experts (labeled “Exp1,” “Exp2”), the cutoff line of 0.7732 sensitivity (horizontal solid line) and the average false positive rate achieved with this criterion (vertical dashed line). Plots for \mathcal{C}_2 and \mathcal{C}_9 present the most linear profile in the middle part of the ROC curve.

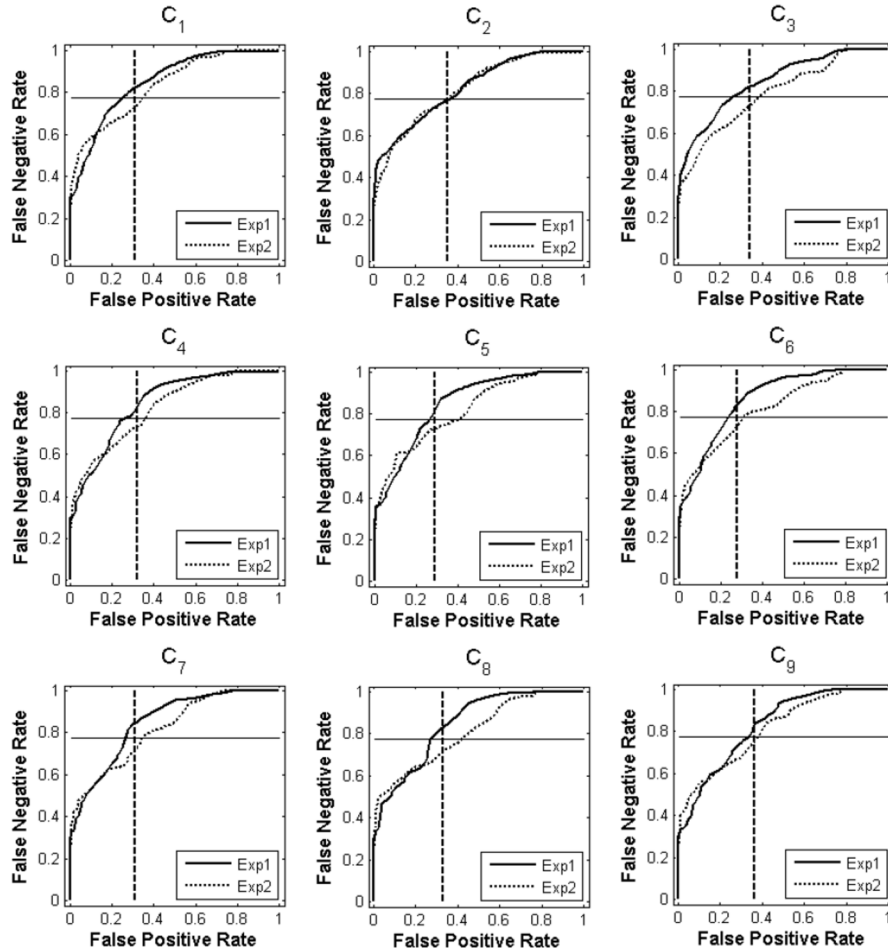


Fig. 9. ROC plots for the nine configurations showing ROC curves for the two experts and the optimal cutoff (horizontal line).

Except for configuration C_3 , which is biased toward Exp1, all configurations agree with Exp2 for high sensitivity (left part of ROC plots) and with Exp1 for medium-high specificity (right part of ROC plots). Concerning cutoff lines, C_5 and C_6 are the best performers in terms of false positive rates (given by vertical dashed lines). The average of the values given by the intersection of the cutoff horizontal line with each expert ROC curve gives our optimal cutoff thresholds, which are $\{1.70, 1.35, 1.40, 2.00, 2.35, 2.35, 2.65, 2.70, 3.45\}$ for C_1C_9 .

Table III reports the statistical scores assessing C_1C_9 , as well as, the comparison to interobserver (IO) variability. We give the average area under ROC curves (AUC), sensitivity (SensRnk) and specificity (SpecRnk) ranges (mean \pm standard deviation, computed for the two experts), confidence interval (SensCI, SpecCI) for mean differences, and Spearman rank correlation (Corr). The top performers for each score are in boldface. Configurations C_5 and C_6 are the ones achieving a best compromise between sensitivity and specificity.

Fig. 10 shows BEPs for the two experts manual labeling and the color map for C_6 . As the interobserver ranges (SensRnk, SpecRnk) of Table III suggest, there is a substantial variability between the two expert labels. The larger disagreement is in the hypertrophic case (Pat.#4) followed by Pat.#5. For the latter, our method performs closer to Expert2, which is identifying injured segments, while Expert1 considers a normal motion. In

general, C_6 achieves a good compromise between both experts, specially for affected segments (sensitivity). The only exception is the basal level of Pat.#7, which is labeled green when both experts consider that it presents an abnormal behavior. However, we note that the classification output is in the transition area (dark colors) between normal and affected. We also observe that apical levels achieve the lowest agreement, with a higher rate of false positive detections (specificity).

VIII. DISCUSSION

A. Model Consistency

Regardless of the dimension, the classifier boundary of the normal group was defined by the ellipsoid containing 95% of the normal samples. Therefore the consistency error should be around 5%. Any increase might be attributed to errors on the computation of the statistical model parameters. The reliability of any statistical analysis drops with either low or dependant number of samples unable to properly explain the variability of the feature space.

In our case, consistency decreases as the dimensionality increases (over 20% for spaces over four dimensions). We attribute such phenomenon to a low number of volunteers ($N_V = 21$) used to compute the statistical model in comparison to the space dimension. Thus, parameter configurations should reach

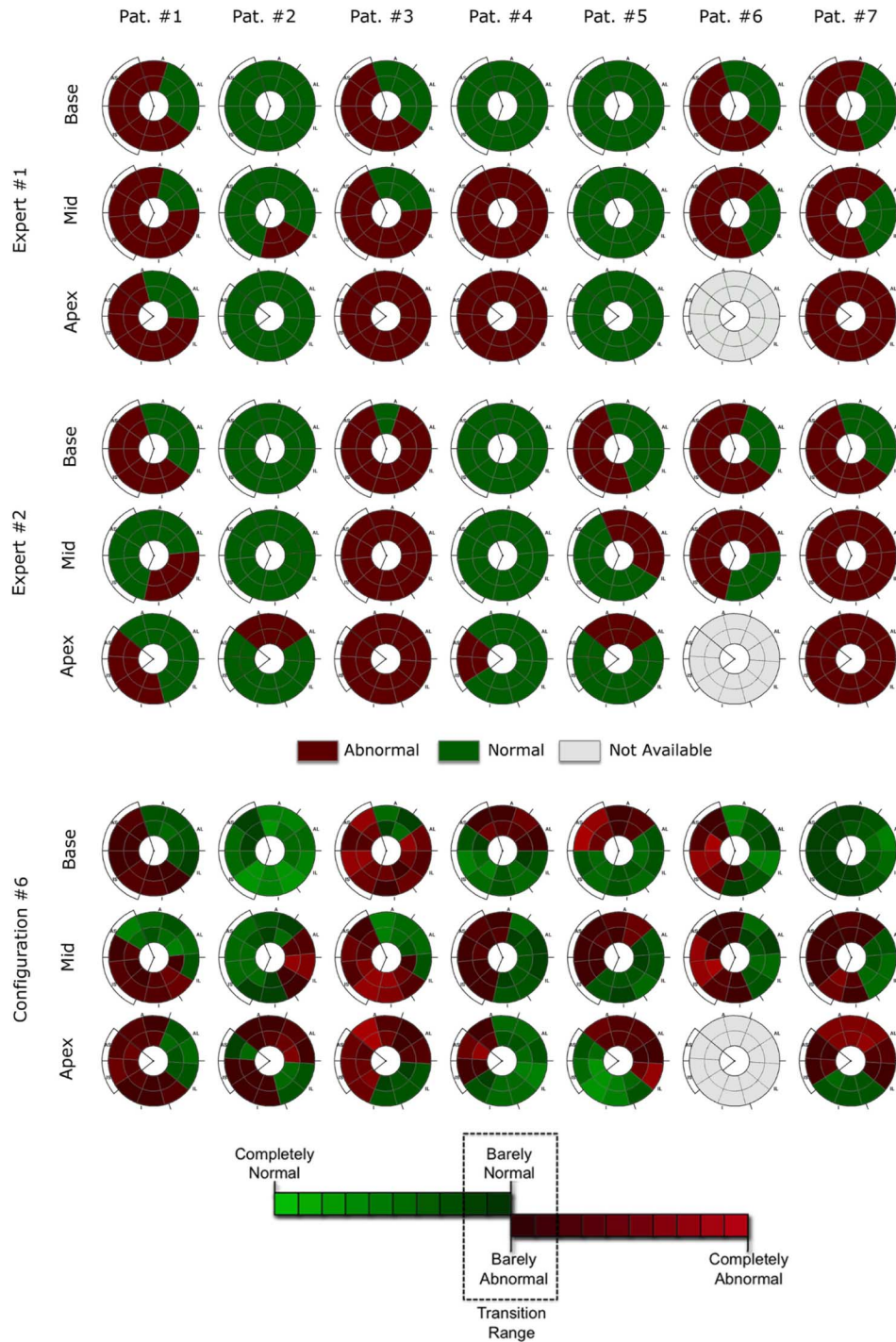


Fig. 10. BEPs for ground truth provided by the clinical experts and classification given by $C_6 = [V_u, V_w, S_M, S_m]$.

the best compromise between number of scores (determined by the number of healthy samples available) and capability for pathology detection. The lower performance of spaces including directional strains is attributed to computational and accumulation errors (they rely on the accuracy of directions estimation).

B. Pathology Discrimination

Table III shows that configurations under five dimensions including motion are favored. This agrees to the fact that visual identification of RWMA strongly relies on motion. In fact,

human experts fail to properly detect areas of abnormal strain, as the hypertrophic Pat.#4 illustrates. It follows that configurations combining strain and motion might improve image-based diagnosis. The configuration achieving the best compromise among the agreement scores considered is C_6 .

Table IV reports for each level (base, mid, and apex) the ranges for accuracy $((TP + TN)/(P + N))$, specificity, and sensitivity obtained by C_6 for their comparison to agreement to visual assessment achieved by the models of normal wall motion reported in [33]. Average percentages for the ICA-based

TABLE III
STATISTICS SUMMARY

	AUC	SensRnk	SpecRnk	SensCI	SpecCI	Corr
C_1	0.86	71.6 ± 29.9	80.7 ± 21.1	(-22.4, 10.9)	(-11.2, 12.9)	0.29
C_2	0.85	73.0 ± 27.1	79.8 ± 20.2	(-19.9, 11.4)	(-11.7, 11.7)	0.26
C_3	0.84	74.2 ± 28.9	76.7 ± 21.4	(-19.4, 13.2)	(-15.3, 9.0)	0.25
C_4	0.86	71.2 ± 29.5	80.1 ± 23.2	(-22.6, 10.4)	(-12.6, 13.1)	0.30
C_5	0.86	75.8 ± 24.3	79.0 ± 27.5	(-16.2, 13.2)	(-15.2, 13.6)	0.27
C_6	0.86	77.6 ± 23.6	76.5 ± 26.1	(-14.2, 14.7)	(-17.2, 10.5)	0.29
C_7	0.85	77.1 ± 25.8	75.1 ± 30.2	(-15.4, 15.0)	(-20.2, 10.7)	0.26
C_8	0.85	74.9 ± 25.5	73.5 ± 30.1	(-17.5, 12.7)	(-21.7, 9.1)	0.22
C_9	0.85	73.8 ± 27.2	75.1 ± 26.5	(-19.2, 12.2)	(-18.8, 9.3)	0.23
IO	-	77.3 ± 29.4	79.8 ± 23.1	-	-	0.39

TABLE IV
RWMA VALIDATION FOR C_6

	AccRnk (%)	SensRnk (%)	SpecRnk (%)
base	70.0 ± 19.5	73.7 ± 32.7	81.6 ± 24.5
mid	65.8 ± 18.8	74.3 ± 21.1	73.3 ± 26.6
apex	63.7 ± 17.0	80.6 ± 22.7	69.9 ± 31.0

TABLE V
RWMA VALIDATION FOR ICA-METHOD AND WT REPORTED IN [33]

	ICA			WT		
	Acc	Sens	Spec	Acc	Sens	Spec
base	63.70	60.83	66.00	70.00	65.83	73.33
mid	67.41	65.12	69.50	68.52	60.47	75.89
apex	66.67	59.42	71.17	62.22	60.87	63.06

method, proposed in [33], and wall thickening (WT) computed using the software developed in [43], are given in Table V. For the apical level, visual identification of anatomical landmarks (especially xant and xinf defining the septal segment) required for NPD definition is sensitive to subjectivity, which drops the model accuracy to 64. However, specificity compares to WT and sensitivity is a 20 higher than ICA and WT. Although mid-level accuracy is a bit lower than ICA and WT, it is the level showing the best compromise between specificity and sensitivity. Sensitivity is higher than ICA and WT, while specificity is between them. Finally, basal level outperforms ICA and WT, achieving the highest specificity (82%).

IX. CONCLUSION AND FUTURE WORK

Determining which clinical scores derived from imaging techniques best detect RWMA is a key point for an accurate diagnosis and follow-up of cardiac diseases. The complex biomechanics of the LV suggest that zeroth- and first-order attributes should be considered. In this paper, we have presented a general framework, the NPD, that allows the fusion and comparison across subjects of different LV local function scores. We illustrate its utility by exploring which regional scores are better suited for RWMA assessment.

The main conclusions derived from our experiments are the following. The NPD framework is a suitable tool for comparison across patients of different local scores. For a set of approximately 20 volunteers, statistical modeling over four dimensions is not reliable. Analysis of BEPs suggests that the output of a system assessing RWMA should be a continuous mapping of the chance that a given region is injured rather than a discrete map grading its abnormal condition. Motion attributes play a central role in accurate detection of RWMA and are well

complemented with extreme strains. In fact, performance of our model combining motion and extreme strains (C_6) compares to state-of-the-art methods.

Although C_6 sensitivity compares to interobserver ranges, its specificity (especially for the apical level) is lower than interobserver variability. Furthermore, for 5% of the sequences (e.g., basal level Pat#7) it fails to detect any injured segments, which hinders its clinical applicability. We consider that the system could be improved in two ways. On one hand, accuracy of RWMA detection is sensitive to \mathcal{LV} boundaries segmentation and definition of regions. In order to reduce the impact of manual identification of landmarks, we are currently developing an automatic segmentation of \mathcal{LV} contours in TMR images including detection of the right-left ventricle septal union (\mathbf{x}_{ant} and \mathbf{x}_{inf}). On the other hand, the normality assumed for statistical models, although suitable for a low number of training samples, might not be the most appropriate for RWMA assessment. This might be addressed by considering other probability distributions for modeling normal function or multiclass approaches for discrimination of specific pathologies (like hypertrophic or asynchronous cases). In any case, a larger number of volunteers and patients are required and it is work that is in progress.

We are also working on the extension of the NPD to 3-D by considering additional anatomic landmarks (apical cap and basal ring) in long-axis slices for the parameterization of the longitudinal direction. This 3-D framework will allow to extend RWMA assessment to the whole ventricular volume. We are using the 3-D NPD to parameterize Diffusion tensor volumes in order to compute a mean model of the myocardial fibers distribution. Such model will be the input for simulations of the LV electromechanical propagation [44].

ACKNOWLEDGMENT

Specially dedicated to Natividad Doria. The authors would like to thank X. Alomar from the Radiology Department of the La Creu Blanca Clinic for providing the tagged sequences.

REFERENCES

- [1] G. Bleumink, A. Knetsch, M. Sturkenboom, S. Straus, A. Hofman, J. D. J. Wittemana, and B. Stricker, "Quantifying the heart failure epidemic: Prevalence, incidence rate, lifetime risk and prognosis of heart failure," *Eur. Heart J.*, vol. 25, no. 18, pp. 1614–1619, 2004.
- [2] R. Tennant and C. Wiggers, "The effect of coronary occlusion on myocardial contraction," *Amer. J. Physiol.*, vol. 112, pp. 351–361, 1935.
- [3] G. Buckberg, "Left ventricular form and function: Scientific priorities and strategic planning for development of new views of disease," *Circulation*, vol. 110, pp. e333–e336, 2004.

- [4] M. Quinones, W. Gaasch, and J. Alexander, "Influence of acute changes in preload, afterload contractile state and heart rate on ejection and isovolumetric indices of myocardial contractility in man," *Circulation*, vol. 53, pp. 293–302, 1976.
- [5] K. Leung and J. Bosch, "Localized shape variations for classifying wall motion in echocardiograms," in *Proc. Med. Image Comput. Comput.-Assist. Interv. (MICCAI)*, 2007, pp. 52–59.
- [6] S. Mansor, N. Hughes, and J. Noble, "Wall motion classification of stress echocardiography based on combined rest-and-stress data," in *Proc. Med. Image Comput. Comput.-Assist. Interv. (MICCAI)*, 2008, pp. 139–146.
- [7] T. Helle-Valle, "New noninvasive method for assessment of left ventricular rotation speckle tracking echocardiography," *Circulation*, vol. 112, pp. 3149–3156, 2005.
- [8] E. Zerhouni, D. Parish, W. Rogers, A. Yang, and E. Shapiro, "Human heart: Tagging with MR imaging—A method for noninvasive assessment of myocardial motion," *Radiology*, vol. 169, no. 1, pp. 59–63, 1988.
- [9] L. Axel and L. Dougherty, "MR imaging of motion with spatial modulation of magnetization," *Radiology*, vol. 171, pp. 841–845, 1989.
- [10] J. Meunier and M. Bertrand, "Ultrasonic texture motion analysis: Theory ND simulation," *IEEE Trans. Med. Imag.*, vol. 14, no. 2, pp. 293–300, Jun. 1995.
- [11] M. Ledesma-Carbayo, J. Derbyshire, S. Sampath, A. Santos, M. Desco, and E. McVeigh, "Unsupervised estimation of myocardial displacement from tagged MR sequences using nonrigid registration," *Magn. Reson. Med.*, vol. 59, no. 1, pp. 181–189, 2008.
- [12] T. Makela, P. Clarysse, O. Sipila, N. Pauna, C. Quoc, T. Katila, and I. Magnin, "A review of cardiac image registration methods," *IEEE Trans. Med. Imag.*, vol. 21, no. 9, pp. 1011–1021, Sep. 2002.
- [13] C. Swingen, R. Seethamraju, and M. Jerosch-Herold, "An approach to the three-dimensional display of left ventricular function and viability using MRI," *Int. J. Cardiovasc. Imag.*, vol. 19, no. 4, pp. 325–336, 2004.
- [14] M. O'Connor, "Evaluation of motion-correction techniques in cardiac SPECT," *J. Nucl. Med.*, vol. 41, no. 7, pp. 580–589, 2000.
- [15] N. Rougon, "A non-rigid registration approach for quantifying myocardial contraction in tagged MRI using generalized information measures," *Med. Imag. Anal.*, vol. 9, pp. 353–375, 2005.
- [16] A. Hennemuth, A. Seeger, O. Friman, S. Miller, B. Klump, S. Oeltze, and H. Peitgen, "A comprehensive approach to the analysis of contrast enhanced cardiac MR images," *IEEE Trans. Med. Imag.*, vol. 27, no. 11, pp. 1592–610, Nov. 2008.
- [17] K. Bhatia, J. Hajnal, B. Puri, A. Edwards, and D. D. Rueckert, "Consistent groupwise non-rigid registration for atlas construction," in *Proc. IEEE Int. Symp. Biomed. Imag.: Nano to Macro*, 2004, pp. 908–911.
- [18] M. Cerqueira, "Standardized myocardial segmentation and nomenclature for tomographic imaging of the heart: A statement for healthcare professionals from the Cardiac Imaging Committee of the Council on Clinical Cardiology of the American Heart Association," *Circulation*, vol. 105, pp. 539–542, 2002.
- [19] N. Rougon, C. Petitjean, F. Preteux, P. Cluzel, and P. Grenier, "A non-rigid registration approach for quantifying myocardial contraction in tagged MRI using generalized information measures," *Med. Imag. Anal.*, vol. 9, no. 4, pp. 353–375, 2005.
- [20] A. Young, B. French, Z. Yang, B. Cowan, W. Gilson, S. Berr, C. Kramer, and F. Epstein, "Reperfusion myocardial infarction in mice: 3D mapping of late gadolinium enhancement and strain," *J. Cardiovasc. Magn. Reson.*, vol. 8, no. 5, pp. 685–692, 2006.
- [21] F. Behloul, B. Lelieveldt, A. Boudraa, M. Janier, D. Revel, and J. Reiber, "Neuro-fuzzy systems for computer-aided myocardial viability assessment," *IEEE Trans. Med. Imag.*, vol. 20, no. 12, pp. 1302–1312, Dec. 2001.
- [22] P. Clarysse, M. Han, P. Croisille, and I. Magnin, "Expository analysis of the spatio-temporal deformation of the myocardium during systole from tagged MRI," *IEEE Trans. Biomed. Eng.*, vol. 49, no. 11, pp. 1328–1339, Nov. 2002.
- [23] F. Bernis, C. Leger, and V. Eder, "Regional analysis of the left ventricle of the heart," *Comput. Med. Imag. Graph.*, vol. 30, no. 3, pp. 153–161, 2006.
- [24] M. Termeer, J. Bescos, M. Breeuwer, A. Vilanova, F. Gerritsen, and M. Grollier, "Covicad: Comprehensive visualization of coronary artery disease," *IEEE Trans. Vis. Comput. Graph.*, vol. 13, no. 6, pp. 1632–1639, Nov.–Dec. 2007.
- [25] W. Lee, Z. Qian, C. Tosti, T. Brown, D. Metaxas, and E. Konofagou, "Preliminary validation of angle-independent myocardial elastography using MR tagging in a clinical setting," *Ultrasound Med. Biol.*, vol. 34, no. 12, pp. 1980–1997, 2008.
- [26] X. Deng and T. Denney, "Three-dimensional myocardial strain reconstruction from tagged MRI using a cylindrical B-spline model," *IEEE Trans. Med. Imag.*, vol. 23, no. 7, pp. 861–867, Jul. 2004.
- [27] X. Deng and T. Denney, "Combined tag tracking and strain reconstruction from tagged cardiac MR images without user-defined myocardial contours," *J. Magn. Reson. Imag.*, vol. 21, no. 1, pp. 12–22, 2005.
- [28] J. Declerck, J. Feldmar, and N. Ayache, "Definition of a four-dimensional continuous planispheric transformation for the tracking and the analysis of left-ventricle motion," *Med. Imag. Anal.*, vol. 2, no. 2, pp. 197–213, 1998.
- [29] W. O'Dell, C. Moore, W. Hunter, E. Zerhouni, and E. McVeigh, "Three-dimensional myocardial deformations: Calculation with displacement field fitting to tagged MR images," *Radiology*, vol. 195, no. 3, pp. 829–835, 1995.
- [30] E. Remme, A. Young, K. Augenstein, B. Cowan, and P. Hunter, "Extraction and quantification of left ventricular deformation modes," *IEEE Trans. Biomed. Eng.*, vol. 51, no. 11, pp. 1923–1931, Nov. 2004.
- [31] A. Rao, R. Chandrashekar, G. Sanchez-Ortiz, R. Mohiaddin, P. Aljabar, J. Hanjnal, B. Puri, and D. Rueckert, "Spatial transformation of motion and deformation fields using non-rigid registration," *IEEE Trans. Med. Imag.*, vol. 23, no. 9, pp. 1065–1076, Sep. 2004.
- [32] J. Bosch, F. Nijland, S. Mitchell, B. Lelieveldt, O. Kamp, J. Reiber, and M. Sonka, "Computer-aided diagnosis via model-based shape analysis automated classification of wall motion abnormalities in echocardiograms," *Acad. Radiol.*, vol. 12, no. 3, pp. 358–367, 2005.
- [33] A. Suinesiaputra, A. Frangi, T. Kaandorp, H. Lamb, J. Bax, and J. R. Lelieveldt, "Automated detection of regional wall motion abnormalities based on a statistical model applied to multislice short-axis cardiac MR images," *IEEE Trans. Med. Imag.*, vol. 28, no. 4, pp. 595–607, Apr. 2009.
- [34] C. Moore, C. Lugo-Olivieri, E. McVeigh, and E. Zerhouni, "Three-dimensional systolic strain patterns in the normal human left ventricle—characterization with tagged MR imaging," *Radiology*, vol. 214, pp. 453–466, 2000.
- [35] J. Garcia-Barnés, D. Gil, S. Pujades, F. Carreras, and M. Ballester, "A normalized parametric domain for the analysis of the left ventricle function," in *Proc. 3rd Int. Conf. Comput. Vis. Theory Appl.*, 2008, vol. 1, pp. 267–274.
- [36] S. Morita, T. Nagase, and K. Nomizu, *Geometry of Differential Forms*, ser. Iwanami Series in Modern Mathematics. Providence, RI: AMS, 2001, vol. 201.
- [37] J. Garcia-Barnés, D. Gil, S. Pujadas, and F. Carreras, "Variational framework for assessment of the left ventricle motion," *Math. Model. Nat. Phenom.*, vol. 3, no. 6, pp. 76–100, 2008.
- [38] J. Milles, A. van Susteren, T. Arts, P. Clarysse, P. Croisille, and I. Magnin, "Automatic 2D segmentation of the left ventricle in tagged cardiac MRI using motion information," in *Proc. IEEE Int. Symp. Biomed. Imag.: Nano Macro*, 2004, pp. 153–156.
- [39] A. Björck, *Numerical Methods for Least Squares Problems*. Philadelphia, PA: SIAM, 1996.
- [40] N. Noble, D. Hill, M. Breeuwer, and R. Razavi, "The automatic identification of hibernating myocardium," in *Proc. Med. Image Comput. Comput.-Assist. Interv. (MICCAI 2004)*, pp. 890–898.
- [41] J. Landis and G. Koch, "The measurement of observer agreement for categorical data," *Biometrics*, vol. 33, pp. 159–174, 1977.
- [42] M. Hollander and D. Wolfe, *Nonparametric Statistical Methods*. New York: Wiley, 1999.
- [43] R. van der Geest, "Comparison between manual and semiautomated analysis of left ventricular volume parameters from short-axis MR images," *J. Comput. Assist. Tomogr.*, vol. 21, no. 5, pp. 756–765, 1997.
- [44] D. Gil, J. Garcia-Barnés, M. Vázquez, R. Aris, and G. Houzeaux, "Patient-sensitive anatomic and functional 3D model of the left ventricle function," presented at the 8th World Congr. Comput. Mech., Venice, Italy, 2008.